# Lower crustal structure in northern California: Implications from strain rate variations following the 1906 San Francisco earthquake

Shelley J. Kenner[1] and Paul Segall

Department of Geophysics, Stanford University, Stanford, California, USA

Received 25 September 2000; revised 20 May 2002; accepted 28 May 2002; published 10 January 2003.

[1] It is well known that geodetic data from a single instant in time cannot uniquely characterize structure or rheology beneath active seismogenic zones. Nevertheless, comparison of spatial and temporal variations in deformation rate with time-dependent mechanical models can place valuable constraints on fault zone geometry and rheology. We consider postseismic strain rate transients by comparing geodetic data from north of San Francisco Bay obtained between 1906 and 1995 to predictions from viscoelastic finite element models. Models include (1) an elastic plate over a viscoelastic half-space, (2) distributed shear within a viscoelastic layer, (3) discrete shear zones within an otherwise elastic layer, (4) discrete shear zones in combination with distributed viscoelastic shear, and (5) midcrustal detachment surfaces. We vary, as applicable, locking depth, elastic thickness, depth to the top and bottom of the distributed shear layer, distributed shear relaxation time, discrete shear zone relaxation time, and discrete shear zone width. The best fitting, physically reasonable elastic plate over viscoelastic half-space models (1) do a poor job simultaneously predicting spatial and temporal variations in the data. The best fitting distributed shear models (2) do a poor job predicting spatial variations in the deformation rate. Although they fit the geodetic data, recent findings from seismic reflection-refraction studies in northern California argue against models with shallow subhorizontal detachments (5). Models incorporating discrete shear zones (3, 4) provide the best fit to the geodetic data and are consistent with seismic studies that argue for discrete fault zones extending through the entire crust. *INDEX TERMS:* 8159 Tectonophysics: Evolution of the Earth: Rheology—crust and lithosphere; 1206 Geodesy and Gravity: Crustal movements—interplate (8155); 1242 Geodesy and Gravity: Seismic deformations (7205); 8164 Tectonophysics: Evolution of the Earth: Stresses—crust and lithosphere; 8158 Tectonophysics: Evolution of the Earth: Plate motions—present and recent (3040); *KEYWORDS:* postseismic, lower crust, California, finite element, San Andreas fault

**Citation:** Kenner, S. J., and P. Segall, Lower crustal structure in northern California: Implications from strain rate variations following the 1906 San Francisco earthquake, *J. Geophys. Res.*, *108*(B1), 2011, doi:10.1029/2001JB000189, 2003.

## 1. Introduction

[2] Nonuniqueness is an inherent problem in modeling geodetic data, especially in strike-slip regimes such as the San Andreas fault system in northern California. The two most common representations of postseismic and interseismic deformation are (1) elastic dislocation models (i.e., thick-skinned models) with kinematically imposed deep slip and (2) elastic plate over viscoelastic half-space models (i.e., thin-skinned models) in which rheology controls the distribution of deformation. For a single fault, it has been shown that these two models cannot be differentiated on the basis of fits to geodetic data [*Savage*, 1990]. The structures and rheologies that control deformation at depth cannot be uniquely determined. Since the physical laws governing stress transfer are not used as additional constraints, some kinematic distribution of slip-rate at depth in elastic dislocation models can always be found which mimics the viscoelastic result. The question is whether or not the equivalent slip distribution is mechanically and rheologically plausible.

[3] In kinematic models, broad postseismic deformation fields can be acceptably fit by placing large amounts of slip at great depth. In naturally time-dependent models, only coseismic slip, rheological parameters, fault constitutive relations, and far-field tectonic boundary conditions are specified. While elastic kinematic inversions for slip at depth are informative, it is far more restrictive to let specified rheologies and fault constitutive relations govern the evolution of the deformation field, as is the case in naturally time-dependent models. Since stress and deformation is concentrated immediately beneath the coseismic rupture, rheological laws significantly limit the depths over which significant postseismic afterslip can occur. Deformation at greater depths and lateral distances results from time-

[1]Now at University of Kentucky, Lexington, Kentucky, USA.


0148-0227/03/2001JB000189$09.00

dependent diffusion of stress away from the source region [e.g., *Thatcher*, 1983; *Li and Rice*, 1987; *Kenner and Segall*, 1999]. Slip distributions predicted by kinematic models are often impossible to reproduce using naturally time-dependent models. Nonlinear rheologies would further concentrate deformation, thereby exacerbating differences between kinematic and naturally time-dependent models.

[4] Problems of nonuniqueness can also be mitigated if a more thorough modeling approach is applied. First, data must have sufficient temporal as well as spatial coverage. Ideally, the data must also document the response of the system to perturbations with widely varying time and length scales. By investigating the response of a system, preferably in three dimensions, to such perturbations, the rheological properties of that system can be more thoroughly explored. Acceptable fault models must satisfactorily explain geodetic observations of both short-term postseismic deformation following a variety of earthquakes and long-term strain accumulation due to steady tectonic loading. They must also satisfy other independent geological and geophysical constraints. Comparison of observed spatial and temporal variations in deformation with naturally time-dependent models can, therefore, limit the number of mechanically plausible fault zone structures and rheologies that fit available observations.

[5] These techniques should be applied whenever possible, but in many regions, including northern California, the geodetic record is limited to a fraction of the earthquake cycle and the spatial coverage, until recently, has not been widespread. Because much of the critical data is based on early triangulation surveys, uncertainties in the resultant strain rate estimates are quite large. Further, realistic mechanical models are time consuming to compute, and knowledge of appropriate material behavior is limited. Nevertheless, many authors have investigated deformation in northern California using elastic dislocation models [e.g., *Thatcher*, 1975a, 1975b; *Savage and Prescott*, 1978; *Prescott and Yu*, 1986; *Lisowski et al.*, 1991; *Lisowski and Savage*, 1992; *Williams et al.*, 1994; *Williams*, 1995; *Murray et al.*, 1998; *Freymueller et al.*, 1999]. Temporal variations in shear strain rates in California have been modeled using both elastic and viscoelastic models [e.g., *Rundle and Jackson*, 1977; *Thatcher*, 1983; *Rundle*, 1986; *Li and Rice*, 1987; *Pollitz and Sacks*, 1992]. More theoretical studies of linear, time-dependent deformation in California, though not directly compared to geodetic data, have been undertaken by *Lehner et al.* [1981], *Cohen* [1982], *Cohen and Kramer* [1984], *Verdonck and Furlong* [1992], and *Furlong and Verdonck* [1994], among others. The effect of nonlinear rheologies during the earthquake cycle has been investigated by *Lyzenga et al.* [1991] and *Reches et al.* [1994]. Most of these studies include only a single fault and do not consider the complete range of possible lower crustal structures. *Kenner and Segall* [2000] describes preliminary modeling of a more complete spatial-temporal data set describing deformation during the ~90 years following the 1906 San Francisco earthquake using simple elastic dislocations models. In this study, we investigate lower crustal structure in northern California (Figure 1) by comparing time-dependent, multiple fault, viscoelastic finite element models with temporal and spatial variations in strain rate derived from geodetic data following the 1906 San Francisco earthquake [*Kenner and Segall*, 2000].

## 2. Data

[6] The data used in this study include triangulation, trilateration, and GPS data spanning the years 1906 to 1995 [*Kenner and Segall*, 2000; *Freymueller et al.*, 1999; *Lisowski and Savage*, 1992]. The data are from two networks: one at Point Arena, California and the other extending from Point Reyes, California to Petaluma, California (Figure 1). At Point Arena the data has been used to infer average shear strain rates for the time periods 1906 to 1930, 1929 to 1975, and 1991 to 1995. Spatially, the Point Arena data is limited to a single, narrow network that spans the San Andreas fault (Figure 2). The Point Reyes-Petaluma arc contains much more spatial information. During two time periods, 1929 to 1939 and 1938 to 1961, we derived an average shear strain rate for each of the subnetworks (Figure 3). During a third time period, 1973 to 1990, the only available shear strain rate estimate is for the subnetwork that spans the San Andreas fault. A more detailed explanation of the data and analysis methods is given by *Kenner and Segall* [2000]. These strain rate estimates improve on earlier data from *Thatcher* [1975a, 1975b, 1983] in that they include more recent measurements as well as all available triangulation data, not simply repeated angles. Using the midpoint of the time interval as a reference, further discussion of these data will be in terms of elapsed time since the 1906 San Francisco earthquake.

[7] Unlike prior studies [*Thatcher*, 1983; *Li and Rice*, 1987] that include data from the San Andreas fault system in both northern and southern California, only data from northern California following the 1906 San Francisco earthquake is considered. Given the limited amount of data and the large uncertainties in the strain rate estimates, we do not consider three-dimensional effects, though lateral variations in material properties at depth are modeled. Despite these limitations, the structure of the lower crust in northern California is a subject of much scientific interest and use of time-dependent viscoelastic models with the complete spatial-temporal data set provides new insights. Diagnostic features of the data which must be matched by appropriate models include (1) initially high peak shear strain rates, (2) significant postseismic effects which persist for decades following the 1906 earthquake, and (3) lateral variations in shear strain rate with distance from the San Andreas fault that also persist for decades.

[8] Shear strain rate estimates initially include contributions from both long-term steady state tectonic loading and postseismic processes [*Kenner and Segall*, 2000]. Unfortunately, multicycle earthquake models with lateral variations in material properties are computationally intensive and techniques for properly applying geologically reasonable far-field tectonic boundary conditions must be refined. In an effort to isolate postseismic perturbations, we therefore subtract contemporary shear strain rates within each subnetwork. Contemporary strain rates are interpolated from observations via a slightly modified version of an elastic dislocation model provided by R. Bürgmann [*Kenner and Segall*, 2000; *Bürgmann et al.*, 1994, 1997]. Deformation

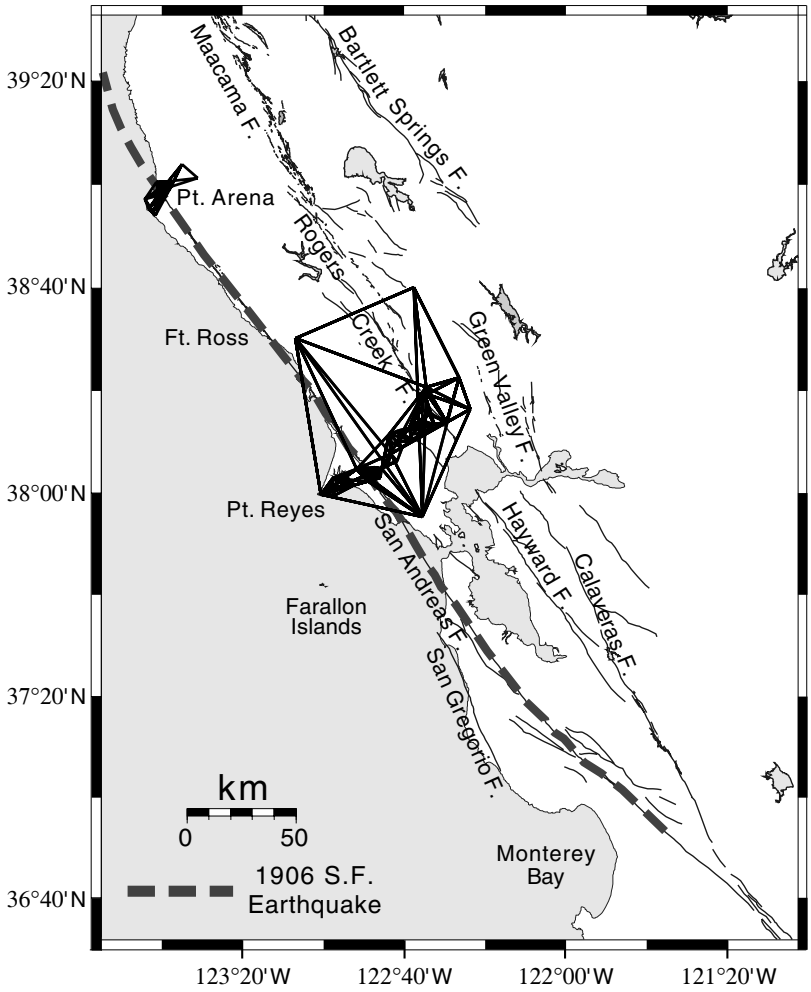


**Figure 1.** General map showing the location of the Point Arena and Point Reyes-Petaluma networks. The trace of the 1906 San Francisco earthquake is shown by the dashed line.

rates predicted by this dislocation model are entirely consistent with modern trilateration and GPS measurements. Use of a thick-skinned dislocation model to estimate steady state rates for use with thin-skinned viscoelastic models is justified as long as the model reasonably represents the steady state behavior. *Segall* [2002] demonstrates the validity of this approximation for models of data from the north San Francisco Bay area. *Segall* [2002] obtains similar results using (1) the total observed deformation rate and a simple model of regularly repeating earthquakes [*Savage and Prescott*, 1978] and (2) the postseismic deformation rate (total minus steady state prediction from the same dislocation model employed here) and a viscoelastic model of the postseismic strain rate decay [*Nur and Mavko*, 1974].

[9] Removal of contemporary strain rates to isolate the postseismic perturbation assumes that contemporary strain rates effectively approximate long-term steady state strain accumulation rates due to tectonic loading and that postseismic transients in the modern day deformation field are negligible. This is consistent with (1) the observed 36 ± 16 year effective relaxation time derived from observations following the 1906 San Francisco earthquake [*Thatcher*,

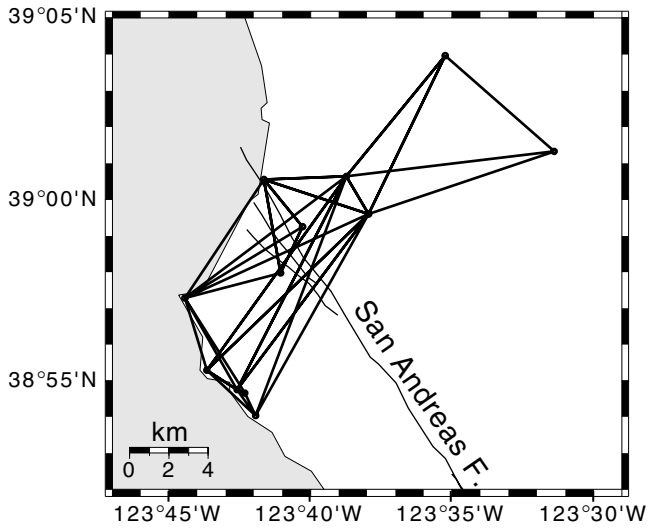


**Figure 2.** Part or all of the Point Arena network was surveyed in 1906–1907, 1925, 1929–1930, and 1973–1975 using triangulation. The majority of the network was resurveyed using GPS between 1991 and 1995.

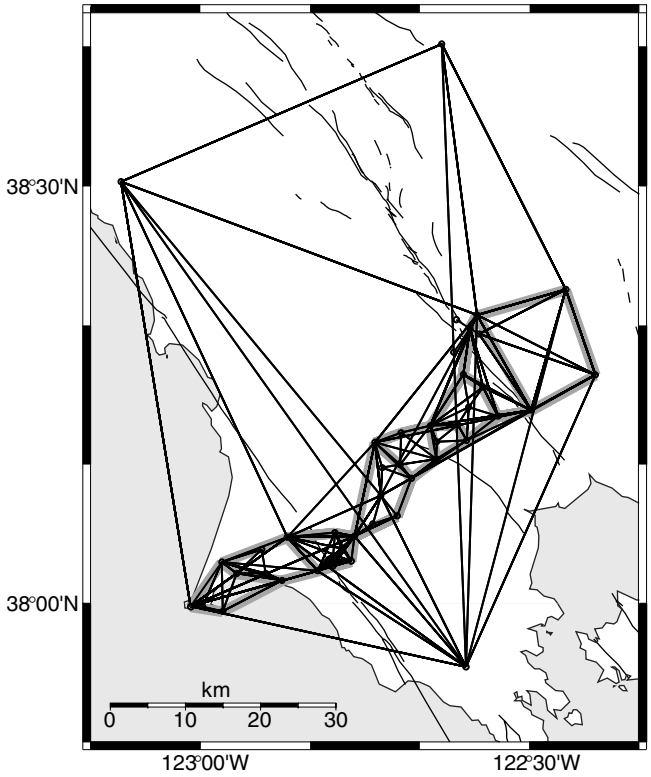


**Figure 3.** The Point Reyes-Petaluma arc was surveyed in 1929–1930, 1938–1939, and 1960–1961 using triangulation. Light gray polygons enclose the subnetworks used to investigate the spatial distribution of shear strain rate within the network. The fault-crossing subnetwork was also surveyed using modern geodetic methods between 1973 and 1991.

1983; *Li and Rice*, 1987; *Kenner and Segall*, 2000], (2) peak deformation rates in the decade following 1906 that are more than 10 times higher than present-day rates [*Thatcher*, 1975a, 1975b; *Kenner and Segall*, 2000], and (3) model results (optimal Type 2-Type 5 models described in this study), which indicate that 90 years after a 1906-type event, postseismic velocity perturbations are everywhere $\leq \sim 3$ mm/yr (e.g., Figure 11). Expected recurrence intervals for the 1906 San Francisco earthquake are between 200 and 300 years. Two hundred years after a 1906-type event, our modeling suggests that postseismic velocity perturbations drop to $\leq \sim 2$ mm/yr with velocities decreasing at a rate of <1 mm/yr per 100 years. As we want to isolate the 1906 postseismic perturbation, removal of residual postseismic signal from events prior to 1906 is advantageous. Since the magnitude of perturbations induced >250 years ago changes extremely slowly, they can be considered constant over the ~90 year interval considered in this study and can be removed with induced errors of <1 mm/yr. Thus, the maximum possible single station error generated by removing the contemporary deformation field is < ~4 mm/yr and probably closer to 3 mm/yr. After 90 years, the postseismic velocity profile is also rather uniform in space (e.g., Figure 11). As a result, errors in strain rate are significantly smaller than peak shear-strain rates observed in the decades immediately following the 1906 earthquake and well within the uncertainties of historical triangulation data.

## 3. Models

[10] As shown by *Kenner and Segall* [1999], we use antiplane finite element models (ABAQUS, *Hibbit, Karlsson & Sorensen, Inc.* [1998]) composed of three-dimensional brick finite and infinite elements. Use of infinite elements approximates a half-space geometry and eliminates difficulties with far-field model boundaries. No tectonic driving forces are applied. Coseismic rupture, 5.5 m of uniform slip along the seismogenic portion of the San Andreas fault, is achieved by defining contact surfaces upon which relative motions are kinematically prescribed. The two surfaces are then locked and the model is allowed to relax. In each model, the lithosphere, composed of elastic and Maxwell viscoelastic elements, overlies a Maxwell viscoelastic half-space representing the mantle. All rheologies are linear and, therefore, superposable. This allows the postseismic stress/strain perturbation to be modeled independently. As described in the previous section, this is consistent with our data processing, which is also designed to isolate the observed postseismic strain rate perturbation.

[11] Five general model types (Figure 4), each characterizing a different hypothesis regarding the nature of deformation in the lower crust and upper mantle in northern California, are considered. Discrete shear zones are modeled as narrow regions of concentrated viscoelastic deformation. When such zones are included, they are placed beneath each of the three subparallel faults in northern California: the San Andreas, Hayward, and Calaveras faults and their northern extensions. Distributed viscoelastic shear layers extend laterally away from the fault to infinity. Locking depth is defined as the maximum depth of coseismic rupture. Applicable rheologies and parameter ranges are given in Table 1.

### 3.1. Type 1

[12] Elastic plate over viscoelastic half-space models (Figure 4a) are simple thin-skinned models of the type investigated by *Thatcher* [1983]. Deformation is broadly distributed below seismogenic depths and variations in

**Figure 4.** (opposite) Model geometry schematics for (a) elastic plate over viscoelastic half-space (Type 1), (b) distributed shear layer (Type 2), (c) discrete shear zones within an otherwise elastic layer (Type 3), (d) discrete shear zones embedded within a distributed shear layer (Type 4a), (e) discrete shear zones in combination with, but not overlapping, a distributed shear layer (Type 4b), and (f) midcrustal detachment (Type 5) models. Where applicable, (g) gives the geometry of the dipping faults [*Parsons and Hart*, 1999]. All dimensions are in km. Converging and diverging arrows denote dimensions that are varied in this study. A black line denotes the coseismic fault. Light gray areas are elastic. Medium gray areas undergo distributed Maxwell viscoelastic deformation. White areas represent discrete Maxwell viscoelastic shear zones. Black areas represent the Maxwell viscoelastic mantle.

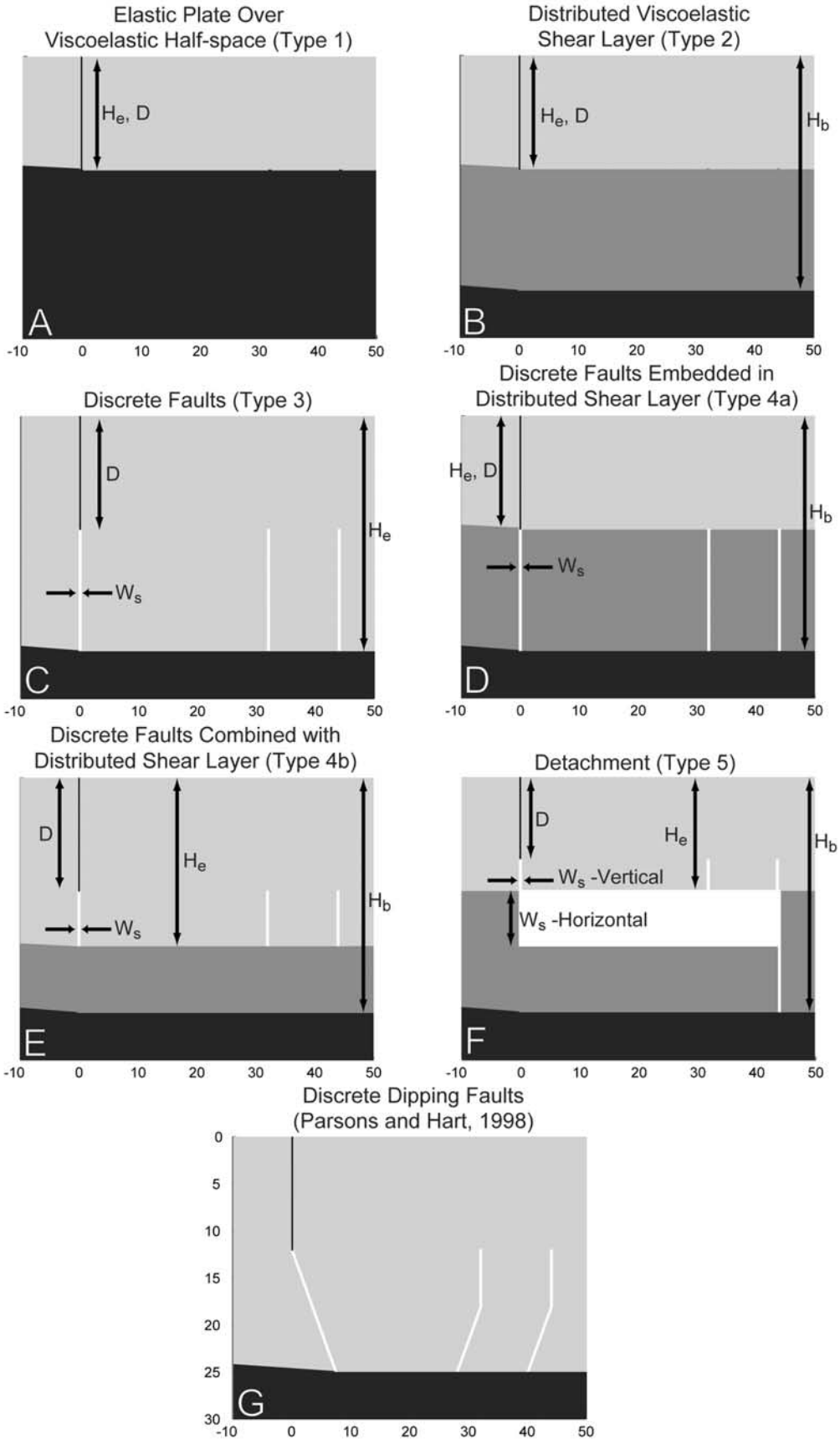
Elastic Plate Over
Viscoelastic Half-space (Type 1)
$H_e$, D
A
Distributed Viscoelastic
Shear Layer (Type 2)
$H_e$, D
$H_b$
B
Discrete Faults (Type 3)
D
$H_e$
$W_s$
C
Discrete Faults Embedded in
Distributed Shear Layer (Type 4a)
$H_e$, D
$H_b$
$W_s$
D
Discrete Faults Combined with
Distributed Shear Layer (Type 4b)
D
$H_e$
$W_s$
$H_b$
E
Detachment (Type 5)
D
$H_e$
$H_b$
$W_s$ -Vertical
$W_s$ -Horizontal
F
Discrete Dipping Faults
(Parsons and Hart, 1998)
G
-10 0 10 20 30 40 50
0 5 10 15 20 25 30

**Table 1.** Model Parameters and Rheologies[a]

| Parameter | Type 1 | Type 2 | Type 3 | Type 4 | Type 5 |
|---|---|---|---|---|---|
| Mantle relaxation time,[b] years | 10–100 | 200[c] | 200[c] | 200[c] | 200[c] |
| Locking depth D, km | = $H_e$ | = $H_e$ | 8, 12, 18 | 8, 12, 18 | 12 |
| Elastic thickness $H_e$, km | 12–45 | 8, 12, 18 | 18, 25, 45, 60 | 8, 12, 18, 25 | 12, 18, 25, 45, 60 |
| Depth to base of distributed shear layer, $H_b$, km | N.A. | 18, 25, 45 | N.A. | 18, 25, 45, 60 | 25, 45, 60 |
| Distributed shear relaxation time,[b] years | N.A. | 1–100 | N.A. | 2–15 | 60–150 |
| Discrete shear zone width $W_s$, km | N.A. | N.A. | 0.2, 0.5, 2.0, 4.0 | 0.5, 2.0 | Horizontal: 6, 7 Vertical: 0.6 |
| Discrete shear zone relaxation time,[b] years | N.A. | N.A. | 0.1–30 | 0.1–30 | 0.25–10 |

[a]Poisson's ratio is uniformly 0.25. The elastic plate and all shear zones have a Young's modulus of 80 GPa. The mantle has a Young's modulus of 150 GPa.
[b]Relaxation time = 2(viscosity/shear modulus).
[c]Corresponds to a viscosity of $\sim 1.9 \times 10^{20}$ Pa s.

viscosity with depth are negligible. In this study, coseismic rupture always extends through the entire elastic layer.

### 3.2. Type 2

[13] In models containing a broadly distributed viscoelastic channel (Figure 4b), deformation is controlled by broadly distributed flow in a weak layer located immediately beneath the seismogenic zone. Flow in the weak layer can effectively decouple the overlying elastic layer from deformation occurring at greater depths. The elastic thickness is always equal to the locking depth.

### 3.3. Type 3

[14] Models containing discrete shear zones within an otherwise elastic layer (Figure 4c) represent a classical thick-skinned approach to crustal deformation. Deformation is localized along narrow, discrete shear zones. The transition from seismic to aseismic slip along the fault plane results from temperature induced changes in the fault frictional properties. Recent seismic studies indicate that discrete shear zones do exist beneath seismogenic zones in California [*Henstock et al.*, 1997; *Hole et al.*, 1998; *Parsons*, 1998; *Parsons and Hart*, 1999; *Zhu*, 2000]. Discrete shear zones extend to the base of the elastic layer.

### 3.4. Type 4

[15] Models containing both discrete shear zones and distributed viscoelastic shear represent an intermediate case in which we include varying amounts of distributed versus discrete deformation. Two Type 4 subcases are considered. In Type 4a models (Figure 4d), discrete shear zones extend to the base of the distributed shear layer and the entire discrete shear zone is embedded within the viscoelastic layer. In Type 4b models (Figure 4e), discrete shear zones do not extend below the top of the distributed shear layer.

### 3.5. Type 5

[16] A final hypothesis is that the Pacific-North American plate boundary at depth is located beneath the Hayward and Calaveras faults. In this instance, a subhorizontal detachment surface (Figure 4f) is proposed which connects to the surface trace of the plate boundary at the San Andreas fault [*Furlong et al.*, 1989]. We assume a detachment thickness of 6 or 7 km. We then vary the depth to the top of the detachment surface (12 & 18 km) as well as those parameters listed in Table 1. Tested models fall into two general classes: those in which the top of the detachment surface is at the base of the seismogenic zone and those in which the top of the detachment surface lies some distance beneath the seismogenic zone. In the second case, coseismic faults connect to the detachment surface via discrete vertical shear zones. All discrete shear zones, whether vertical or horizontal, have the same relaxation time. A viscoelastic distributed shear layer may be included which extends to the top of the detachment surface.

### 3.6. Dipping Faults

[17] Dipping fault geometries (Figure 4g) are investigated for model types 3 and 4a using the geometry suggested by *Parsons and Hart* [1999] from seismic reflection surveys in San Francisco Bay. Their work only constrains the geometry of the San Andreas and Hayward faults at depth. We assume the geometry of the Calaveras fault is similar to that of the Hayward fault. If the shear zones extend below 25 km depth, they are vertical. In total over 550 different combinations of parameters were investigated [*Kenner*, 2000].

## 4. Model Fit to Data

[18] To accurately compare geodetically derived strain rates with those inferred from the finite element models we approximate the procedures used to analyze the actual geodetic data in both the temporal and spatial domains [*Kenner and Segall*, 2000]. Strain rates calculated from the geodetic data are based on position estimates made during two or more surveys. Differences in position between the surveys are then used to calculate average deformation rates over the time intervals considered. While the finite element program can output strain rates at any time, we calculate model strain rates from strain output at the beginning and end of the relevant time period. Using the notation in Table 2, at a given node, the strain rate during each time interval, $m$, becomes

$$\dot{\varepsilon}_m = \frac{\varepsilon|_{t_f^m} - \varepsilon|_{t_i^m}}{t_f^m - t_i^m}. \quad (1)$$

Though this approach is not entirely correct for comparison to modern trilateration and GPS measurements, which generally infer average deformation rates using more than two surveys, time-dependent variations in strain rate are not significant after $\sim$1960. In contrast, strain rates inferred from triangulation data were determined using data from only two, or at most three, surveys [*Kenner and Segall*, 2000]. Thus, during the time periods in which postseismic transients are most pronounced, the finite element estimates of deformation rate satisfactorily represent the time-averaged nature of the actual data.

**Table 2.** Definitions of Variables

| Variable | Definition |
|---|---|
| $\varepsilon$: | Model strain at node points |
| $\dot{\varepsilon}_m$: | Model strain rate at node points for time interval $m$ |
| $\dot{\varepsilon}'_m$: | Interpolated strain rate at the uniformly spaced model points for time interval $m$ |
| $\dot{\varepsilon}'_{nm}$: | Average interpolated model strain rate for time period $m$ and network $n$ |
| $\dot{\varepsilon}^g_{nm}$: | Geodetically determined strain rate estimate for time period $m$ and network $n$ |
| $\sigma_{nm}$: | Standard deviation of geodetically determined strain rate for time period $m$ and network $n$ |
| $\Sigma$: | Diagonal matrix of geodetically determined strain rate variances |
| D: | Coseismic locking depth |
| $e_{nm}$: | Model residual for time period $m$ and network $n$ |
| $e^{norm}_{nm}$: | Model normalized residual for time period $m$ and network $n$ |
| $e_{avg}$: | Average model residual (model misfit) |
| **E**: | Vector of model residuals $\mathbf{e}_{nm}$ |
| $H_b$: | Depth to the base of the distributed shear layer |
| $H_e$: | Depth to the base of the elastic layer |
| k: | Total number of strain rate estimates |
| $t$: | Time |
| $t^m_i$: | Time of initial survey in estimate of geodetic deformation rate during time period $m$ |
| $t^m_f$: | Time of final survey in estimate of geodetic deformation rate during time period $m$ |
| $W_s$: | Discrete shear zone width |
| $x^n_{NE}$: | Northeastern extent of network $n$ |
| $x^n_{SW}$: | Southwestern extent of network $n$ |
| $x'$: | Fault perpendicular distance from the San Andreas fault of the uniformly spaced model points |

[19] Spatially, the anti-plane finite element models specify strain rates along a linear, irregularly spaced profile of node points. Using geodetic data, we obtain average strain rates for small networks of irregularly spaced stations in two dimensions. To correlate these results we use a linear interpolation scheme to resample the nodal strain rates, $\dot{\varepsilon}_m$, along a regularly spaced grid of points, $x'$, to obtain $\dot{\varepsilon}_m$. Then, for each geodetic strain rate estimate, $\dot{\varepsilon}^g_{nm}$, we calculate the spatial average of the model strain rate over the fault perpendicular distance spanned by network $n$, during time period $m$,

$$\dot{\varepsilon}'_{nm} = \mathrm{avg}\left(\dot{\varepsilon}'_m\right) \; \forall \; x^n_{SW} \le x' \; \le \; x^n_{NE}. \tag{2}$$

If the finite element output is not resampled, the node spacing in the finite element grid can bias the average model strain rate estimate for the network.

[20] The normalized model residual for each strain rate estimate is given by

$$e^{norm}_{nm} = \frac{e_{nm}}{\sigma_{nm}} = \frac{\dot{\varepsilon}^g_{nm} - \dot{\varepsilon}'_{nm}}{\sigma_{nm}}, \tag{3}$$

while the average normalized residual, a.k.a. the $L_2$ model misfit, becomes

$$e_{avg} = \sqrt{\frac{E^T \Sigma^{-1} E}{k}}, \tag{4}$$

where E, $\Sigma$, and k are defined in Table 2. $e_{avg}$ is heavily weighted toward years that have the most spatial data (i.e., the largest number of data points), mainly 28 and 43.5 years after the 1906 San Francisco earthquake. As a result, the $L_2$ measure of misfit masks reasonable fits to temporal variations in strain rate, thereby reducing the discriminatory power of the data set. In particular, though we have only a single strain rate determination for a fault-crossing network at 11.5 years post-1906, this data provides a critical model constraint. The data from which this point is derived have been used without reservation in prior studies that consider only the temporal evolution of peak shear strain rates. [*Thatcher*, 1983; *Li and Rice*, 1987]. In an effort to give equal emphasis to both temporal and spatial constraints, we therefore refer to the maximum normalized residual $(e^{norm}_{nm})_{max}$, the $L_\infty$ norm, in subsequent discussions. Realizing that this approach places great emphasis on outliers, we neglect, when noted, the two most obvious outliers. These anomalous measurements, both occurring 28 years after the 1906 earthquake (at x = −13 km and x = 22 km in Figures 6–10), have been attributed to possible observational errors and problems with the subnetwork geometry [*Thatcher*, 1975b; *Cline et al.*, 1985; *Kenner and Segall*, 2000]. Because they are not consistent with the spatial trends seen in the rest of the 28-year Point Reyes-Petaluma arc data, we feel this approach is reasonable.

[21] Balanced use of both spatial and temporal data via analysis of the maximum normalized residual is a particularly important criterion for discriminating between different models of the same type. When comparing the best fitting models of each type, trends in average and maximum

**Table 3.** Optimal Models

| Model Type | Maximum Normalized Residual ($L_\infty$ norm) | Average Normalized Residual ($L_2$ norm) |
|---|---|---|
| Type 1 | 4.3[a] | 2.376[a] |
| Type 2 | 3.1 | 1.792 |
| Type 3: vertical | 2.7[b,c] | 1.446[b,c] |
| Type 3: dipping | 2.4[c] | 1.484[c] |
| Type 4a: vertical | 2.3[c] | 1.497[c] |
| Type 4a: dipping | 2.5[c] | 1.523[c] |
| Type 4b: vertical | 2.7[c] | 1.709[c] |
| Type 5 | 2.4[c] | 1.354[c] |

[a]For physically reasonable locking depths/crustal thicknesses.
[b]For a physically reasonable locking depth of 12 km. Slightly better misfits are obtained for shallower locking depths.
[c]Excludes to two outliers in the 28-year data.

normalized residual are more coherent. The maximum and average normalized misfits for all optimal models are given in Table 3. Differences of ~0.3 in the maximum normalized residual often result in qualitatively insignificant changes in the model fit to the data. Since more data is included in the assessment, variations > ~0.15–0.2 in average normalized residual do generate discernable changes in the qualitative fit to the data, even if differences in maximum normalized residual are in the range given above. Before comparing the various models, note that the maximum normalized residual cannot be < ~2.3 because this value splits the difference between strain rates observed in fault-crossing subnetworks at 43.5 and 46 years. The 43.5-year data is from the Point Reyes-Petaluma arc and the 46-year data is from the Point Arena network. The difference between the two may represent along strike variations in postseismic deformation rate following the 1906 San Francisco earthquake or simply the accuracy of the data.

### 4.1. Elastic Plate Over Viscoelastic Half-Space (Type 1) Models

[22] We limit the range of possible elastic plate over viscoelastic half-space models to those with elastic thicknesses/locking depths of ≤25 km based on estimates of the depth of coseismic slip at Point Arena [*Thatcher*, 1975a; *Thatcher et al.*, 1997; *Matthews and Segall*, 1993]. With this constraint, the optimal model, which has an elastic thickness/locking depth of 25 km and a mantle relaxation time of 40 years, has a maximum normalized residual of 4.3 (Figures 5a and 6). Variations in peak shear strain rate at the trace of the San Andreas fault with time are very poorly reproduced. Specifically, high strain rates observed 11.5 years post-1906 are not matched. Smaller elastic thicknesses/locking depths or longer mantle relaxation times lead to serious misfits of peak shear strain rates. Relaxation times ≤ ~20 years do a better job fitting the temporal evolution of peak shear strain rates at the San Andreas fault but cannot fit the spatial data. In general, elastic plate over viscoelastic half-space models have much higher normalized residuals than other model types (Table 3).

### 4.2. Distributed Shear Layer (Type 2) Models

[23] Models incorporating a distributed shear layer (Type 2) are more appropriate. The best fitting model, which has an elastic thickness/locking depth of 18 km, a distributed shear relaxation time of 5 years, and $H_b$ = 60 km, has a maximum normalized residual (excluding the two outliers in the 28 year data set) of 3.1 (Figures 5b and 7). For an elastic thickness/locking depth of 18 km and shear layer relaxation times between ~1 to ~5 years (effective Maxwell viscosities of $5.0 \times 10^{17}$ to $2.5 \times 10^{18}$ Pa s), the results are not particularly sensitive to $H_b$. There are models with $L_\infty \leq$ ~3.3 for the entire range of geometrically reasonable $H_b$ (22–60 km). Other elastic thicknesses/locking depths and longer relaxation times yield significant misfits during at least one time period, with particular difficulties seen for data at 11.5 and 43.5 years. In all cases, low viscosities manifest themselves as very high initial shear strain rates followed by very little temporal variation in the deformation rate and extremely broad, spatially uniform strain rate profiles (Figures 5b and 7). Although uncertainties in the data are large, this deformation history does not capture

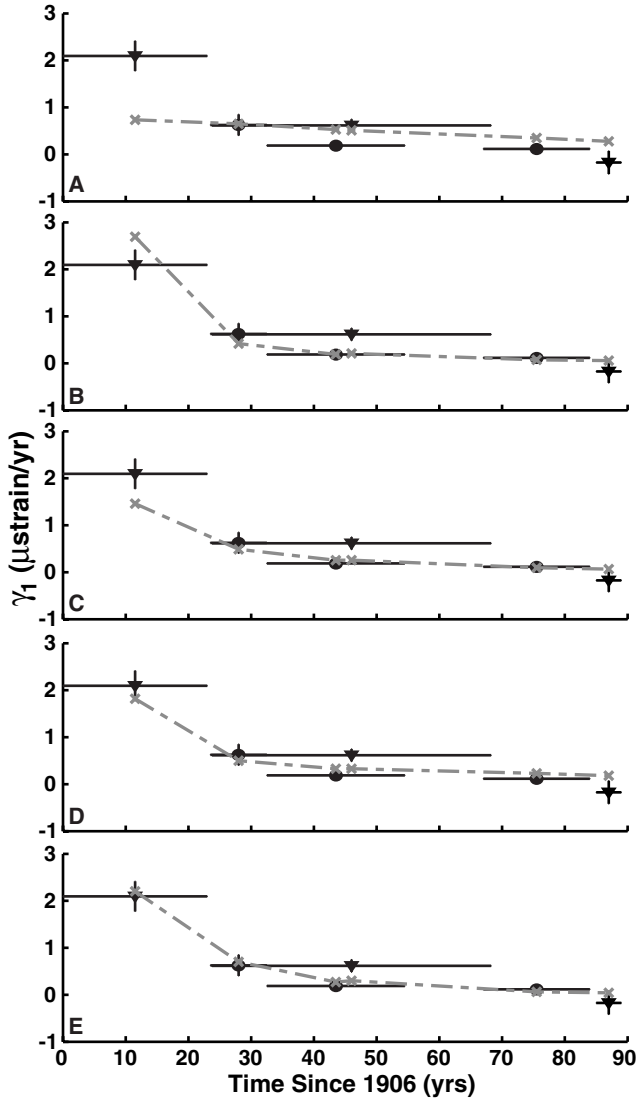


**Figure 5.** Comparison of the model results and observed peak shear strain rates within small fault-crossing subnetworks for the best fitting (a) elastic plate over viscoelastic half-space (Type 1), (b) distributed shear layer (Type 2), (c) discrete shear zones within an otherwise elastic layer (Type 3), (d) discrete shear zones embedded within a distributed shear layer (Type 4a), and (e) midcrustal detachment (Type 5) models. Model descriptions and fits to the spatial data are given in Figures 6–10. Symbols give the average postseismic shear strain rate from the Point Arena network (triangles) and the Point Reyes-Petaluma arc (circles). For each observation, the crosses give the model result averaged over the same temporal and spatial scale (section 4). For interpretation purposes, a dashed line connects the model points. Since average finite element strain rates are calculated from strains at the beginning and end of the actual observation interval (equations (1) and (2)) deformation rates at 46 years (1929–1975, Point Arena) may be slightly higher than those at 43.5 years (1938–1961, Point Reyes-Petaluma).

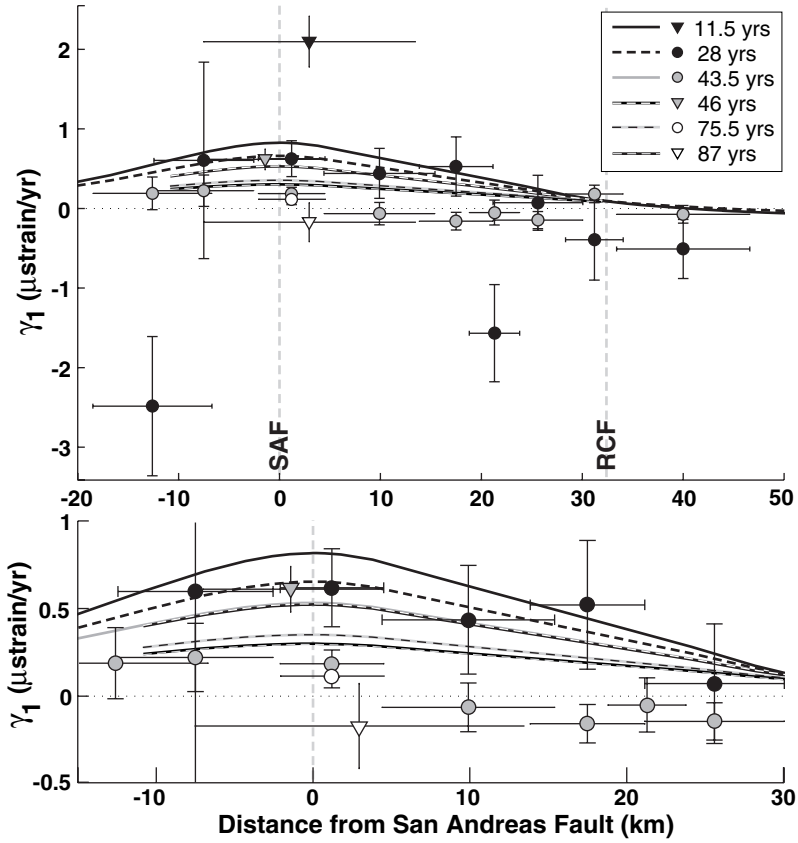


**Figure 6.** Best fitting, geometrically reasonable elastic plate over viscoelastic half-space model (Type 1). The elastic thickness/locking depth is 25 km. The mantle relaxation time is 40 years. Symbols give the average postseismic shear strain rate from the Point Arena network (triangles) and subnetworks of the Point Reyes-Petaluma arc (circles). Vertical error bars give 1σ uncertainty in the magnitude. Horizontal error bars give the lateral extent, in the fault parallel direction, of each subnetwork. Since average finite element strain rates are calculated from strains at the beginning and end of the actual observation interval (equations (1) and (2)) deformation rates at 46 years (1929–1975, Point Arena) may be slightly higher than those at 43.5 years (1938–1961, Point Reyes-Petaluma). Solid lines give resampled finite element model results. Due to decreasing rates of change in shear strain rate, the 43.5 and 46 year and 75.5 and 87 year model line may overlap. To help alleviate this problem, the upper figure shows all the data. The lower figure gives a closer view of strain rate variations near the San Andreas fault later in the earthquake cycle.

the behavior of the observed deformation field, especially the decrease in shear strain rates toward the Rogers Creek/Hayward fault. Thus, although Type 2 models can predict the decay in peak shear strain rates with time, they do a poor job predicting spatial variations with distance from the San Andreas fault.

### 4.3. Discrete Shear Zones Within an Otherwise Elastic Layer (Type 3) Models

[24] The best fitting models which contain discrete shear zones within an otherwise elastic layer (Type 3) have locking depths of 8 km, are not sensitive to elastic thickness within the ranges investigated, and have discrete shear zone relaxation times of ~0.5 to ~1 years for a shear zone width of 0.5 km. These models have an $L_\infty$ norm (excluding outliers) of 2.4–2.5. Based on studies of coseismic deformation during the 1906 earthquake, an 8 km locking depth is presumably too shallow [*Thatcher*, 1975a; *Thatcher et al.*, 1997; *Matthews and Segall*, 1993]. For a 12 km locking depth with 0.5 km wide shear zones, the best geometrically reasonable model has a maximum normalized residual (excluding outliers) of 2.7, an elastic thickness of 60 km, and a shear zone relaxation time of 0.5 years (Figures 5c and 8). For the same locking depth, an elastic thickness of 45 km, and shear zone relaxation time of 1 year, the fit is degraded to $L_\infty$ = 3.0 (excluding outliers). Severe underestimates of peak shear strain rates immediately following the 1906 earthquake (11.5 years) cause model misfits to degrade as elastic thickness is decreased. This problem is more pronounced for locking depths of 18 km where, even for elastic thicknesses of 60 km, the best model has a maximum normalized residual of only 3.6.

[25] Discrete shear zones effectively localize deformation at depth. In the optimal Type 3 model (Figures 5c and 8), relative postseismic displacement across the shear zone beneath the San Andreas fault at 34 km is ~2.5 m 200 years after the 1906 earthquake. For the considered parameter ranges, there is a distinct trade-off between shear zone width and relaxation time. Geodetic data is only sensitive to relative motion across the shear zone. For thicknesses

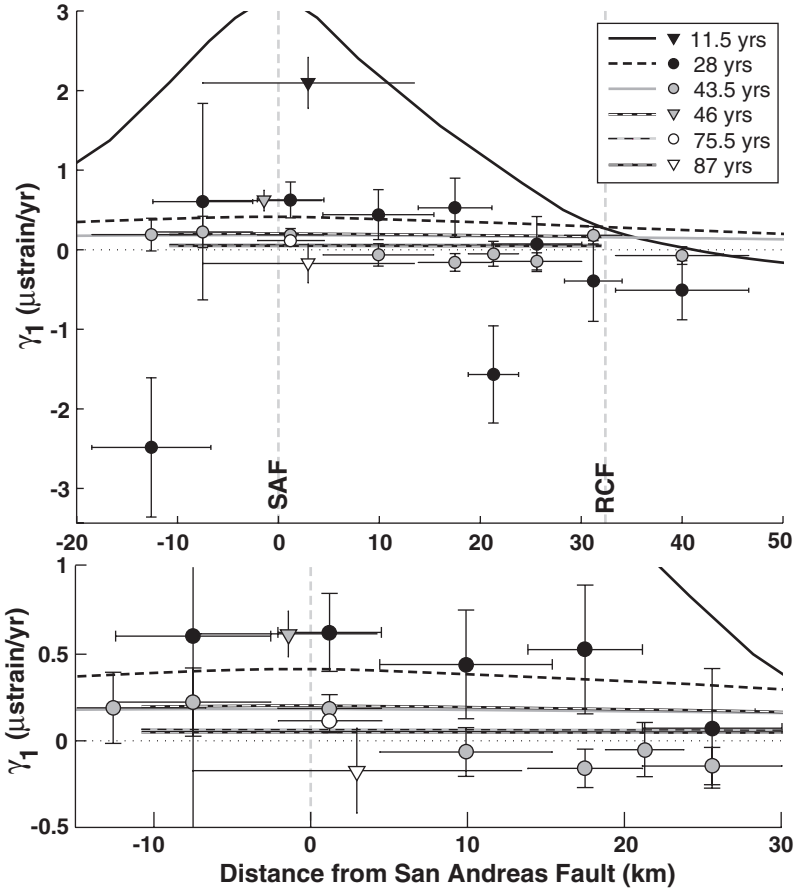


**Figure 7.** Best fitting distributed shear layer model (Type 2). The elastic thickness/locking depth is 18 km, $H_b$ = 60 km, and the distributed shear relaxation time is 5 years. A figure description and symbol definitions are given in Figure 6.

narrower than the resolution of the geodetic data the ratio of viscosity to shear zone thickness is all that is discernible. At the surface, relative displacement rates across a high viscosity, wide shear zone will be similar to rates above a narrow shear zone with lower viscosity [*Linker and Rice*, 1997]. Given available geodetic data, our modeling indicates that this relation begins to break down for shear zone widths greater than ~5 km. At this point, the viscosity is too high and deformation is too diffuse to match the high shear strain rates immediately following the 1906 San Francisco earthquake.

### 4.4. Discrete and Distributed Shear Combination (Type 4) Models

[26] Models containing both discrete shear zones and distributed shear (Type 4) are intermediate between Type 2 and Type 3 models. In fact, there are two distinct minima in the misfit space corresponding to these end-member cases. Within each local minima we see the same, previously identified trends. All presented Type 4 models have a shear zone width of 0.5 km. As with the Type 3 models, there is a trade-off between shear zone relaxation time and thickness for thicknesses less than ~5 km.

[27] In models in which the discrete shear zone is completely embedded within the distributed shear layer (Type 4a), the best fitting models approach the Type 3 end-member. The optimal model fit has a maximum normalized residual of 2.3 (excluding outliers) for a locking depth of 12 km, $H_b$ = 60 km, and a distributed shear relaxation time of 150 years (Figures 5d and 9). An equally good fit is obtained for $H_b$ = 45 km and a distributed shear relaxation time of 100 years. Both have a discrete shear zone relaxation time of 0.25 years. For a 18 km locking depth, the best model has an $L_\infty$ norm of 2.8 (excluding outliers) for $H_b$ = 60 km, a distributed shear relaxation time of 100 years, and a discrete shear zone relaxation time of 0.25 years. These models fit slightly better than their Type 3 (i.e., discrete shear zones embedded within an elastic layer) equivalents.

[28] For Type 4a models with locking depth held fixed, as $H_b$ is reduced model rheologies shift and eventually approach the Type 2 (i.e., distributed shear layer) end-member. With an 18 km locking depth, if $H_b$ is reduced to 25 km, the best fitting model misfit is $L_\infty$ = 3.4 with a distributed shear relaxation time of 2 years and a discrete shear zone relaxation time of 0.25 years. For a 12 km locking depth, if $H_b$ = 18 km, the optimal model misfit is $L_\infty$ = 3.8 with the same relaxation times.

[29] Models in which the discrete shear zones do not extend below the top of the distributed shear layer (Type 4b) are only considered for a locking depth of 12 km and an elastic thickness of 25 km. This is in the optimal parameter

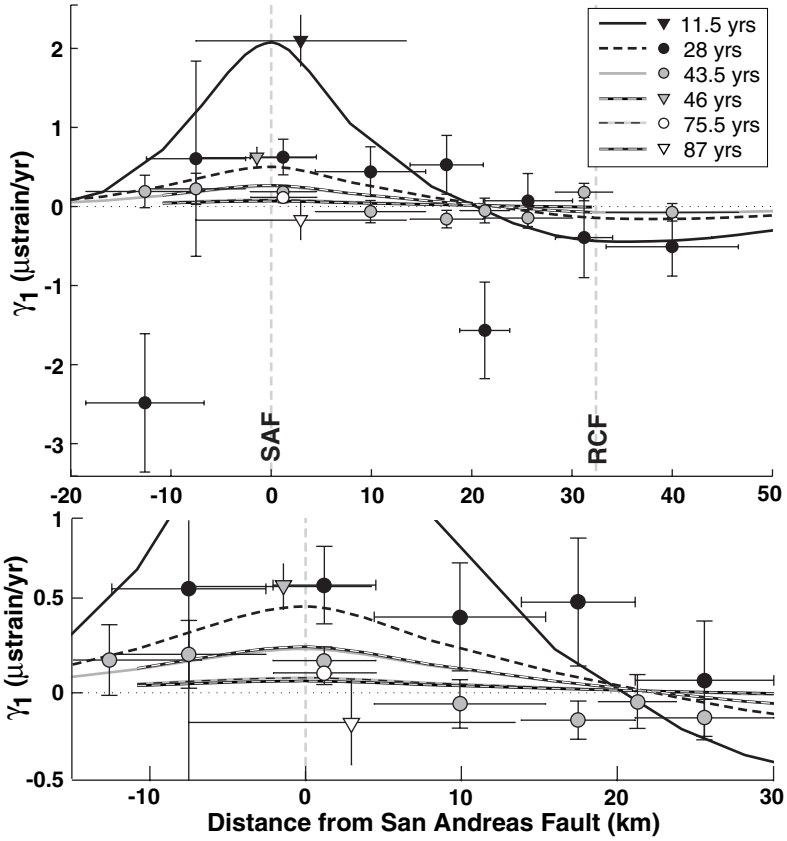


**Figure 8.** Best fitting, geometrically reasonable model containing discrete, vertical shear zones within an otherwise elastic layer (Type 3). This model has a locking depth of 12 km, an elastic thickness of 60 km, a shear zone width of 0.5 km, and a discrete shear zone relaxation time of 0.5 years. A figure description and symbol definitions are given in Figure 6.

range suggested by *Li and Rice* [1987] using modified Elsasser models with similar geometry and a combined geodetic data set from both northern and southern California. Given these parameter choices, we find that the optimal Type 4b models do not fit the strain rate data as well as the best fitting Type 4a models though the differences are minimal (Table 3). The optimal Type 4b model has a distributed shear relaxation time of 80 years, a discrete shear zone relaxation time of 0.5 years, $H_b$ = 60 km, and a maximum normalized residual of 2.7 (excluding outliers).

### 4.5. Detachment (Type 5) Models

[30] Models with shear along a midcrustal detachment (Type 5) are generally insensitive to rheology below the detachment, as the detachment effectively decouples the elastic upper crust from material below it. Only a 12 km locking depth is considered. For the case in which the top of the detachment is located at the base of the seismogenic zone, optimal models have an $L_\infty$ misfit of 3.5. They possess discrete shear zone relaxation times of 2–5 years and distributed shear relaxation times >100 years. Models in which an elastic material replaces the distributed shear layer fit the data equally well. For the case in which the detachment is connected to the seismogenic faults via vertical, discrete shear zones, the maximum normalized misfit for the optimal model is 2.4 (excluding outliers) with a discrete shear zone relaxation time of 1 year and an elastic layer below the detachment (Figures 5e and 10). In contrast to observations, discrete shear zone relaxation times of <1 year yield initially high shear strain rates that quickly taper off to a fairly constant value in both space and time. Though the possibility is not investigated here, detachment models may represent a proxy for distributed shear that is limited in lateral extent by the main subparallel faults in the region.

### 4.6. Dipping Faults

[31] Given the resolution of the data, dipping fault zones do not change our results significantly. For models containing discrete shear zones embedded within an elastic layer (Type 3), the parameters from the optimal vertical fault model (12 km locking depth) give $L_\infty$ = 2.4 (excluding outliers) for dipping faults versus 2.7 (excluding outliers) for vertical faults. If a distributed shear layer is included (Type 4a), the optimal 12 km locking depth parameter set yields $L_\infty$ = 2.5 (excluding outliers) for dipping faults versus 2.3 (excluding outliers) for the vertical fault case. Surface deformation profiles do differ, however, especially as distributed shear layer relaxation times become long (i.e., the material approaches the elastic limit). With dipping faults, deformation profiles are more asymmetric with respect to the trace of the San Andreas fault. Slightly higher positive postseismic strain rates are seen at and just west of the San Andreas fault. Slightly higher negative strain rates are seen at the trace of the Rogers Creek/Hayward fault. As

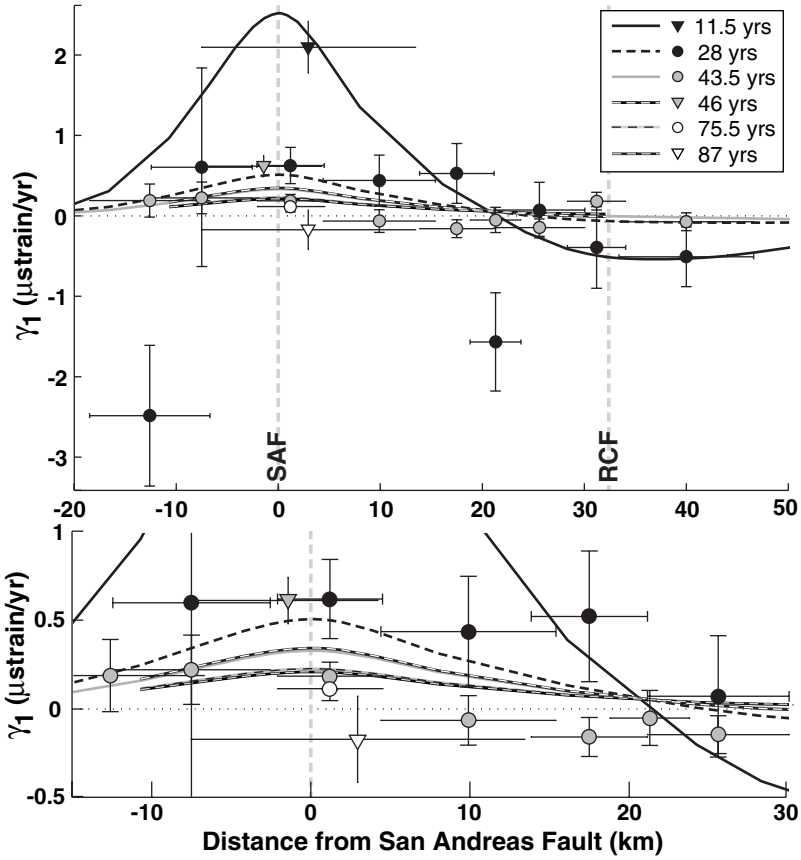


**Figure 9.** Best fitting model containing discrete, vertical shear zones embedded within a viscoelastic layer (Type 4a). The model has a locking depth of 12 km, $H_b$ = 60 km, a distributed shear relaxation time of 150 years, a discrete shear zone width of 0.5 km, and a discrete shear zone relaxation time of 0.25 years. A figure description and symbol definitions are given in Figure 6.

seen in the surface velocity profiles (Figure 11), dipping faults enhance postseismic deformation rates between the major subparallel faults in northern California.

[32] Even more pronounced is the effect of dipping faults on the distribution of the postseismic stress perturbation at depth. When the faults are vertical, the layer between the seismogenic elastic crust and the viscoelastic mantle is transitional between areas of postseismic stress decrease in the seismogenic crust and areas of postseismic stress increase in the mantle (Figure 12a). With dipping faults, the area of greatest stress decrease extends to the top of the mantle east of the San Andreas fault. Similarly, the area of greatest stress increase extends to the base of the seismogenic zone immediately west of the San Andreas fault (Figure 12b). Though these differences change reloading rates on the San Andreas fault only slightly, the presence of dipping faults slows postseismic stress recovery on subparallel faults to the east.

## 5. Discussion

[33] Based on the model fits that we obtained, the following inferences can be made. First, the model types which best fit the available geodetic data following the 1906 San Francisco earthquake include discrete shear zones (Types 3–5), whether or not a distributed shear layer is included. In all cases, both the temporal and spatial fit to the available geodetic data (Figures 5–10) is more appropriate than for models that do not contain discrete shear zones (Types 1–2). Discrete shear zone relaxation times must be extremely short, <1–2 years (effective Maxwell viscosity of $5.0 \times 10^{17}$–$1 \times 10^{18}$ Pa-s) for viscosity/thickness ratios capable of fitting the available data both temporally and spatially. Unfortunately, seismic reflection data cannot place any independent constraints on the widths of these shear zones [*Parsons*, 1998; *Parsons and Hart*, 1999]. The top of the discrete shear zone must be located within 10–18 km of the surface to generate the initially high deformation rates observed immediately following the earthquake.

[34] A point of concern may be that the optimal Type 3 and Type 4a models contain discrete shear zones extending to 45 or 60 km depth, while the Moho in this region is at ~25 km. Further, if discrete shear zones are confined to the upper 25 km, Type 3 and 4 models cannot be differentiated from distributed shear layer (Type 2) models on the basis of misfit. First, it should be noted that the lithosphere/asthenosphere boundary along the San Andreas fault in northern California is inferred to be at between 50 and 60 km depth [*Zandt and Furlong*, 1982]. As a result, shear zones that extend to 45 or 60 km may not be completely unrealistic. Second, consider Type 3 models with discrete shear zones embedded within an elastic layer. As elastic thickness is

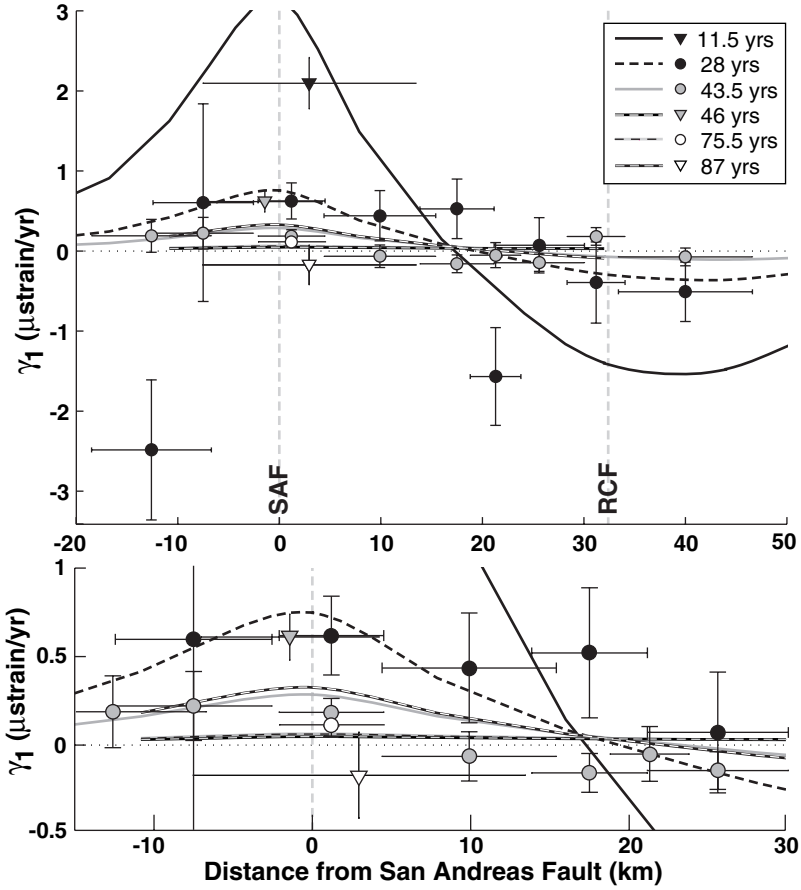


**Figure 10.** Best fitting detachment model (Type 5). This model has a locking depth of 12 km, an elastic thickness of 60 km, a vertical shear zone width of 0.5 km, and a horizontal detachment thickness of 7 km. The top of the detachment is at 18 km depth. Discrete shear zones have a relaxation time of 1 year. There is no distributed shear layer in this model. A figure description and symbol definitions are given in Figure 6.

reduced, fits to the temporal data degrade and misfits approach those of the optimal distributed shear layer (Type 2) model. Unlike optimal Type 2 models, however, spatial variations in deformation rate are still present. We know that postseismic and interseismic deformation in northern California is asymmetric with respect to the trace of the San Andreas fault [*Kenner and Segall*, 2000; *Freymueller et al.*, 1999]. Given similar misfits, therefore, even nonoptimal discrete shear zone models (Type 3; Type 4a approaching a Type 3 end-member) are still preferred. Other models cannot generate sufficient asymmetry.

[35] Although the postseismic responses are very different [*Kenner and Segall*, 1999], models containing discrete vertical shear zones (Types 3 & 4) and subhorizontal detachment surfaces (Type 5) cannot be differentiated solely on the basis of the existing geodetic data set (Table 3). Even with slightly better data and more advanced modeling techniques, independent information will be necessary to discriminate among these model types. Within the San Andreas fault system, evidence for the existence of discrete vertical or dipping shear zones that cut through the entire crust has been found in a growing number of seismic studies [*Hole et al.*, 1998]. In particular, such evidence has been found in northern California [*Henstock et al.*, 1997], in the San Francisco Bay region [*Parsons*, 1998; *Parsons and Hart*, 1999], and in southern California [*Zhu*, 2000]. Based on this evidence, we feel that models with discrete vertical shear zones (Types 3 and 4) provide the best description of lower crustal structure in northern California.

[36] A second conclusion is that optimal models of post-1906 deformation include rheologies with at least two different relaxation times. The lack of fit using elastic plate over viscoelastic half-space models (Type 1) clearly shows this. Thus, in addition to discrete shear zones with short relaxation times, there must exist a structure with a relaxation time > ~100 years (effective Maxwell viscosity of $9.5 \times 10^{19}$ Pa-s). This can take the form of distributed shear in the lower crust and/or upper mantle. Long-period deformation sources of this type continually drive deformation along structures with shorter relaxation times located nearer the surface. When short relaxation time structures are located beneath each of the three subparallel faults in the region, spatial variations in the deformation field are also generated. In purely linear models, rheological interactions of this type are required to match variations in surface deformation rate in both space and time. Incorporation of nonlinear rheologies may allow for this type of behavior as well, but such models have not yet

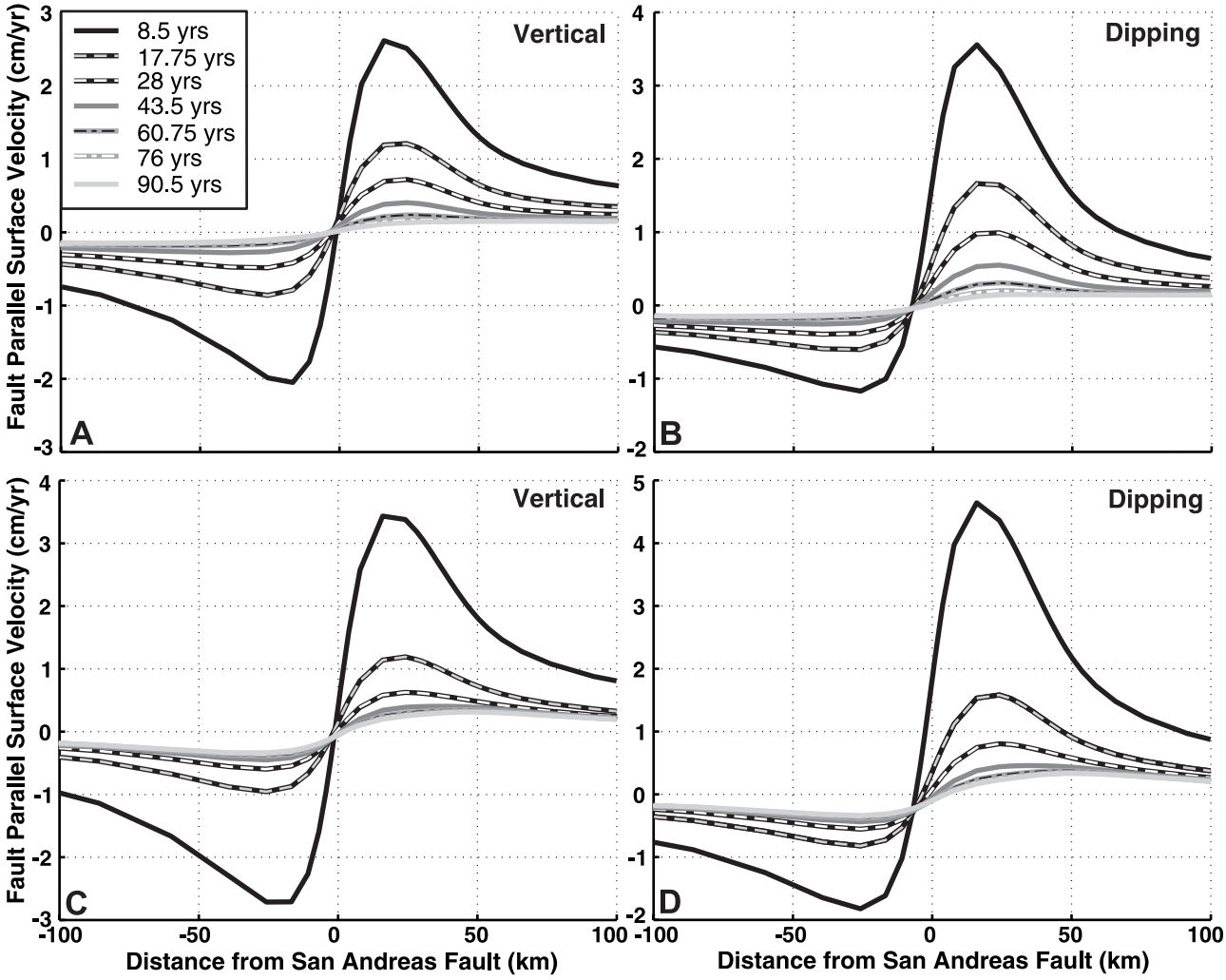


**Figure 11.** Postseismic surface velocity perturbation profiles showing the effect of dipping, discrete fault zones for (a & b) the Type 3 models described in Figure 8 and (c & d) the Type 4a models described in Figure 9. (a) and (c) show results with vertical fault. (b) and (d) give velocities for the dipping fault case.

been explored. *Tse and Rice* [1986] demonstrate that nonlinear fault constitutive relations specified along discrete faults at depth are capable of producing temporal variations in peak, fault-crossing shear strain rate similar to those seen in the northern California post-1906 data.

[37] Based on modeling that indicates at least two relaxation times (or nonlinear rheologies) must be present, we can conclude that estimates of effective relaxation time based on geodetic data after large events are just that: estimates of *effective* relaxation time. The measurements actually reflect the combined influence of structures having multiple relaxation times. Prior estimates of effective Maxwell relaxation time following great events on the San Andreas fault range from 30 to 40 years [*Thatcher*, 1983; *Li and Rice*, 1987; *Kenner and Segall*, 2000]. When a single 30-year relaxation time is used, resultant Type 1 models do not fit the combined temporal-spatial postseismic data set, regardless of locking depth. Geodetic estimates of effective relaxation time, therefore, represent some average decay time that represents the multitude of interacting processes that are likely to occur within geometrically complex fault systems.

[38] Finally, it may be noted that our results differ slightly from the results of previous studies. Many factors contribute to these variations. Prior modeling of post-1906 deformation [*Thatcher*, 1983; *Li and Rice*, 1987] matched results to temporal variations in total strain rate, not just the postseismic perturbation. In contrast to this investigation, the *Thatcher* [1983] and *Li and Rice* [1987] studies combine data from both northern and southern California. Inclusion of additional geodetic data in northern California and its subsequent reanalysis using the methods of *Yu and Segall* [1996] has also led to updated northern California strain rates [*Kenner and Segall*, 2000]. Finally, and most significantly, neither previous study attempts to match spatial data from the 2–4 decades immediately following great earthquakes on the San Andreas fault.

[39] More specifically, *Thatcher* [1983] uses an elastic plate over viscoelastic half-space (Type 1) model to infer a relaxation time following great events on the San Andreas fault. Only temporal variations in peak shear strain rate are used in the inversion. Based on the depth of coseismic faulting in 1906, a 10 km elastic thickness is used and a relaxation time of ~30 years is inferred. For

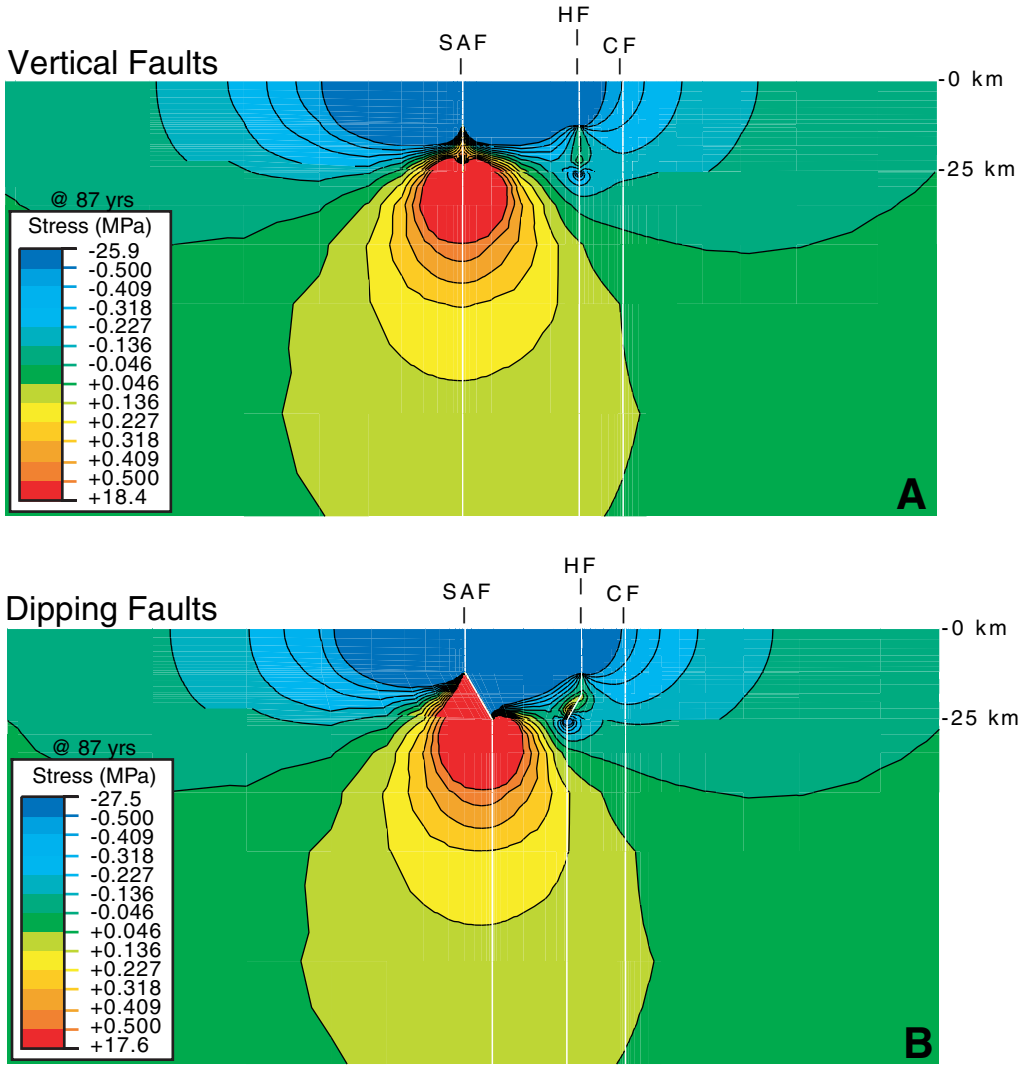


**Figure 12.** Contour plots of the postseismic shear stress perturbation 87 years after the coseismic event for a model containing discrete shear zones embedded within an elastic layer (Type 3). The locking depth is 12 km, the elastic thickness is 25 km, the shear zone width is 0.5 km, and the discrete shear zone relaxation time is 2 years. The results compare the effect of (a) vertical versus (b) dipping discrete shear zones.

typical lithospheric shear moduli, this corresponds to a viscosity of $\sim 3 \times 10^{19}$ Pa-s. Using these parameter choices and the postseismic strain rate perturbation data used in this study, a maximum normalized residual of 11.0 ($L_2$ norm of 3.456) is obtained. Since the elastic thickness/locking depth is so small, both the 28 and 43.5 year spatial data are severely overestimated.

[40] *Li and Rice* [1987] use a modified Elsasser model that includes a freely slipping surface connecting the coseismic San Andreas fault and an underlying viscoelastic channel. Reasonable model fits to temporal variations in peak shear strain rate following great earthquakes on the San Andreas fault give channel viscosities of $2 \times 10^{18} - 2 \times 10^{19}$ Pa-s. These multicycle models also acceptably predict contemporary spatial variations in the deformation field. To further investigate the postseismic behavior of *Li and Rice* [1987] type models, we note that they are analogous to Type 4b models since the freely slipping surface behaves like a discrete shear zone that relaxes instantaneously. Thus, the *Li and Rice* [1987] models contain structures with two different relaxation times. Using locking depths and elastic thicknesses that are comparable to the preferred geometries given by *Li and Rice* [1987], we obtain satisfactory fits to the northern California data. The best fitting Type 4b models cannot be distinguished from other models containing discrete vertical shear zones (Type 3, 4a) on the basis of available geodetic observations (Table 3). In the best fitting Type 4b models, our inferred distributed shear layer viscosities are $3 \times 10^{19} - 4 \times 10^{19}$ Pa-s, only slightly higher than the values suggested by *Li and Rice* [1987].

## 6. Conclusions

[41] In summary, we find that 90 years of post-1906 geodetic data in northern California are best explained by

models which include discrete vertical shear zones within the lower crust beneath each of the three subparallel faults in the region (Types 3 & 4). Models that incorporate discrete detachment surfaces (Type 5) fit the data equally well but do not agree with independent information obtained from seismic reflection studies. Models that incorporate only distributed viscoelastic deformation (Types 1 & 2) cannot generate the appropriate spatial distribution of deformation.

[42] To match the available geodetic data in both space and time using linear rheologies, optimal models need to contain lower crust/upper mantle structures that have at least two different relaxation times. At least one of the relaxation times needs to be relatively short ($\leq \sim$1 year). At least one of the others needs to be much longer ($\geq \sim$100 years). With this combination, a single major earthquake can generate initially high postseismic strain rates during the first 1–2 decades after the event that persist at subdued yet measurable levels for 40–50 years. Alternatively, this result may be indicative of prevalent nonlinear material behavior at depth.

[43] Finally, the effect of dipping faults cannot be discerned in the post-1906 data. This does not mean, however, that the presence of dipping discrete faults does not have a profound effect on the nature of the postseismic deformation field. Dipping, discrete faults produce significant changes in the spatial distribution of the postseismic stress perturbation below seismogenic depths. Rather than being a region with little or no concentration of stress, dipping faults act to asymmetrically concentrate stress along the downdip extension of the coseismic fault. This changes the surface deformation field, making it more asymmetric. It also alters the rate at which neighboring faults recover from postseismic stress decreases induced by the initial earthquake.

[44] **Acknowledgments.** We thank Mark Murray for his advice and help in incorporating the GPS data and Roland Bürgmann for the use of his secular deformation model. Steve Cohen, William Prescott, and the associate editor provided beneficial reviews. This work was supported by USGS grant 1434-HQ-97-GR-03122.

## References

Bürgmann, R., R. Arrowsmith, T. Dumitru, and R. McLaughlin, Rise and fall of the southern Santa Cruz Mountains, California, deduced from fission track dating, geomorphic analysis, and geodetic data, *J. Geophys. Res.*, *99*, 20,181–20,202, 1994.

Bürgmann, R., P. Segall, M. Lisowski, and J. Svarc, Postseismic strain following the 1989 Loma Prieta earthquake from GPS and leveling measurements, *J. Geophys. Res.*, *102*, 4933–4955, 1997.

Cline, M. W., R. A. Snay, and E. L. Timmerman, Geodetically derived strain from the San Francisco bay to the Mendocino triple junction, California, *NOAA Tech. Rep. NOS 109 NGS 31*, 17 pp., Natl. Oceanic and Atmos. Admin., Silver Springs, Md., 1985.

Cohen, S. C., A multilayer model of time dependent deformation following and earthquake on a strike slip fault, *J. Geophys. Res.*, *87*, 5409–5421, 1982.

Cohen, S. C., and M. J. Kramer, Crustal deformation, the earthquake cycle, and models of viscoelastic flow in the asthenosphere, *Geophys. J. R. Astron. Soc.*, *78*, 735–750, 1984.

Freymueller, J. T., M. H. Murray, P. Segall, and D. Castillo, Kinematics of the Pacific-North American Plate Boundary Zone, northern California, *J. Geophys. Res.*, *104*, 7419–7441, 1999.

Furlong, K. P., and D. Verdonck, Three-dimensional lithospheric kinematics in the Loma Prieta region, California: Implications for the earthquake cycle, in *The Loma Prieta, California, Earthquake October 17, 1989 - Tectonic Processes and Models*, edited by R. W. Simpson, *U.S. Geol. Surv. Prof. Pap. 1550-F*, F103–F131, 1994.

Furlong, K. P., W. D. Hugo, and G. Zandt, Geometry and evolution of the San Andreas fault zone in northern California, *J. Geophys. Res.*, *94*, 3100–3110, 1989.

Henstock, T. J., A. Levander, and J. A. Hole, Deformation in the lower crust of the San Andreas fault system in northern California, *Science*, *278*, 650–653, 1997.

Hibbit, Karlsson & Sorensen, Inc., *ABAQUS User's Manual, Version 5.8*, vol. 1–3, Pawtucket, R. I., 1998.

Hole, J. A., B. C. Beaudoin, and T. J. Henstock, Wide-angle seismic constraints on the evolution of the deep San Andreas plate boundary by Mendocino triple junction migration, *Tectonics*, *17*, 802–818, 1998.

Kenner, S. J., Mechanical modeling of time dependent deformation in the lower crust and its effect on earthquake recurrence, Ph.D. thesis, Stanford Univ., Stanford, Calif., 2000.

Kenner, S. J., and P. Segall, Time-dependence of the stress shadowing effect and its relation to the structure of the lower crust, *Geology*, *27*, 119–122, 1999.

Kenner, S. J., and P. Segall, Postseismic deformation following the 1906 San Francisco earthquake, *J. Geophys. Res.*, *105*, 13,195–13,209, 2000.

Lehner, F. K., V. C. Li, and J. R. Rice, Stress diffusion along rupturing plate boundaries, *J. Geophys. Res.*, *86*, 6155–6169, 1981.

Li, V. C., and J. R. Rice, Crustal deformation in great California earthquake cycles, *J. Geophys. Res.*, *92*, 11,533–11,551, 1987.

Linker, M. F., and J. R. Rice, Models of postseismic deformation and stress transfer associated with the 1989 Loma Prieta earthquake, in *The Loma Prieta, California, Earthquake of October 17, 1989 - Postseismic Effects, Aftershocks, and Other Phenomena*, edited by P. A. Reasenberg, *U.S. Geol. Surv. Prof. Pap.*, *1550-D*, D253–D275, 1997.

Lisowski, M., and J. C. Savage, The velocity field in the San Francisco bay area and the inferred depth of creep on the Hayward fault, in *Proceedings of the Second Conference on Earthquake Hazards in the Eastern San Francisco Bay Area*, *Spec. Publ. 113*, edited by G. Borchardt et al., pp. 39–44, Calif. Dep. of Conserv., Div. of Mines and Geol., Sacramento, 1992.

Lisowski, M., J. C. Savage, and W. H. Prescott, The velocity field along the San Andreas fault in central and southern California, *J. Geophys. Res.*, *96*, 8369–8389, 1991.

Lyzenga, G. A., A. Raefsky, and S. G. Mulligan, Models of recurrent strike-slip earthquake cycles and the state of crustal stress, *J. Geophys. Res.*, *96*, 21,623–21,640, 1991.

Matthews, M. V., and P. Segall, Estimation of depth-dependent fault slip from measures surface deformation with application to the 1906 San Francisco earthquake, *J. Geophys. Res.*, *98*, 12,153–12,163, 1993.

Murray, M. H., W. H. Prescott, R. Bürgmann, J. T. Freymueller, P. Segall, J. Svarc, S. D. P. Williams, M. Lisowski, and B. Romanowicz, The deformation field of the Pacific-North American plate boundary zone in northern California from geodetic data, 1972–1998 (abstract), *EOS Trans. AGU*, *79*, Fall Meet. Suppl., F192, 1998.

Nur, A., and G. Mavko, Postseismic viscoelastic rebound, *Science*, *183*, 204–206, 1974.

Parsons, T., Seismic-reflection evidence that the Hayward fault extends into the lower crust of the San Francisco Bay area, California, *Bull. Seismol. Soc. Am.*, *88*, 1212–1223, 1998.

Parsons, T., and P. E. Hart, Dipping San Andreas and Hayward faults revealed beneath San Francisco Bay, California, *Geology*, *27*, 839–842, 1999.

Pollitz, F. F., and I. S. Sacks, Modeling of postseismic relaxation following the great 1857 earthquake, southern California, *Bull. Seismol. Soc. Am.*, *82*, 454–480, 1992.

Prescott, W. H., and S. Yu, Geodetic measurement of horizontal deformation in the northern San Francisco bay region, California, *J. Geophys. Res.*, *91*, 7475–7484, 1986.

Reches, Z., G. Schubert, and C. Anderson, Modeling of periodic great earthquakes on the San Andreas fault: Effects of nonlinear crustal rheology, *J. Geophys. Res.*, *99*, 21,983–22,000, 1994.

Rundle, J. B., An approach to modeling present-day deformation in southern California, *J. Geophys. Res.*, *91*, 1947–1959, 1986.

Rundle, J. B., and D. D. Jackson, A kinematic viscoelastic model of the San Francisco earthquake of 1906, *Geophys. J. R. Astron. Soc.*, *50*, 441–458, 1977.

Savage, J. C., Equivalent strike-slip earthquake cycles in half-space and lithosphere-asthenosphere earth models, *J. Geophys. Res.*, *95*, 4873–4879, 1990.

Savage, J. C., and W. H. Prescott, Asthenospheric readjustment and the earthquake cycle, *J. Geophys. Res.*, *83*, 3369–3376, 1978.

Segall, P., Integrating geologic and geodetic estimates of slip rate on the San Andreas fault system, *Int. Geol. Rev.*, *44*(1), 62–82, 2002.

Thatcher, W., Strain accumulation and release mechanism of the 1906 San Francisco earthquake, *J. Geophys. Res.*, *80*, 4862–4872, 1975a.

Thatcher, W., Strain accumulation on the northern San Andreas fault zone since 1906, *J. Geophys. Res.*, *80*, 4873–4880, 1975b.

Thatcher, W., Nonlinear strain buildup and the earthquake cycle on the San Andreas fault, *J. Geophys. Res.*, *88*, 5893–5902, 1983.

Thatcher, W., G. Marshall, and M. Lisowski, Resolution of fault slip along the 470-km-long rupture of the great 906 San Francisco earthquake and its implications, *J. Geophys. Res.*, *102*, 5353–5367, 1997.

Tse, S. T., and J. R. Rice, Crustal earthquake instability in relation to the depth variation of frictional slip properties, *J. Geophys. Res.*, *91*, 9452–9472, 1986.

Verdonck, D., and K. P. Furlong, Stress accumulation and release at complex transform plate boundaries, *Geophys. Res. Lett.*, *19*, 1967–1970, 1992.

Williams, S. D. P., Current motion on faults of the San Andreas system in central California inferred from recent GPS and terrestrial survey measurements, Ph.D. thesis, Univ. of Durham, Durham, England, 1995.

Williams, S. D. P., J. L. Svarc, M. Lisowski, and W. H. Prescott, GPS measured rates of deformation in the northern San Francisco bay region, California, 1990–1993, *Geophys. Res. Lett.*, *21*, 1511–1514, 1994.

Yu, E., and P. Segall, Slip in the 1868 Hayward earthquake from the analysis of historical triangulation data, *J. Geophys. Res.*, *101*, 16,101–16,118, 1996.

Zandt, G., and K. P. Furlong, Evolution and thickness of the lithosphere beneath coastal California, *Geology*, *10*, 276–381, 1982.

Zhu, L., Crustal structure across the San Andreas fault, Southern California from teleseismic converted waves, *Earth Planet. Sci. Lett.*, *179*, 183–190, 2000.

S. J. Kenner, Department of Geological Sciences, University of Kentucky, 101 Slone Building, Lexington, KY 40506-0053, USA. (skenner@uky.edu)

P. Segall, Department of Geophysics, Stanford University, Stanford, CA 94305-2215, USA. (segall@stanford.edu)